International Journal of Mechanical System Dynamics

WILEY

IJMSD International Journal of Mechanical System Dynamics Open Access

RESEARCH ARTICLE OPEN ACCESS

Machine Learning-Assisted Sensitivity Analysis for Stochastic Fatigue Life Modeling of Metals

Tran C. H. Nguyen[1] | N. Vu-Bac[2,3]

[1]Reactor Center, Dalat Nuclear Research Institute, Dalat, Vietnam | [2]Faculty of Civil Engineering, Ho Chi Minh University of Technology (HCMUT), Ho Chi Minh City, Vietnam | [3]Vietnam National University Ho Chi Minh City, Linh Trung Ward, Ho Chi Minh City, Vietnam

Correspondence: N. Vu-Bac (vbnam@hcmut.edu.vn)

Received: 15 January 2025 | **Revised:** 4 March 2025 | **Accepted:** 25 March 2025

Funding: We acknowledge Ho Chi Minh City University of Technology (HCMUT), VNU-HCM for supporting this study.

Keywords: fatigue life prediction | machine learning | multiaxial loading | parameter dependency | variance-based sensitivity analysis

ABSTRACT

Predicting fatigue life with precision requires more than isolated evaluations of mechanical properties; it requires an integrated approach that captures the interdependencies between various parameters, including elastic modulus, tensile strength, yield strength, and strain-hardening exponent. Neglecting these correlations in sensitivity analyses can compromise prediction accuracy and physical interpretability. In this study, we introduce a dependency-aware sensitivity analysis framework, assisted by machine learning-based surrogate models, to evaluate the contributions of these mechanical properties to fatigue life variability. Tensile strength emerged as the most influential parameter, with significant second-order interactions, particularly between tensile and yield strength, highlighting the central role of coupled effects in fatigue mechanisms. By addressing these interdependencies, the proposed approach improves the reliability of fatigue life predictions and offers a solid foundation for the optimization of metallic components subjected to cyclic stresses.

1 | Introduction

Fatigue remains one of the most significant failure mechanisms in metallic structures, particularly for components subjected to cyclic loading [1]. Unlike static failures, fatigue is characterized by the progressive accumulation of damage, often culminating in sudden and catastrophic fractures after prolonged exposure to repeated stress cycles. This phenomenon is especially concerning in metallic components, which are foundational in aerospace, automotive, and civil engineering applications due to their high strength, ductility, and versatility [2, 3]. Metals, while advantageous for their load-bearing capacity, exhibit microstructural behaviors under cyclic stresses, such as slip band formation and grain boundary degradation, that render them particularly susceptible to fatigue-related damage [4, 5]. These failures frequently occur without visible precursors, under nominally safe stress levels, and are exacerbated by multiaxial loading conditions.

In reality, loading is rarely uniaxial. Multiaxial fatigue involves simultaneous stresses along different axes, introducing complex interactions between normal and shear stress that significantly influence crack initiation and propagation. The challenge is further amplified under nonproportional loading, where phase differences between stress components induce additional cyclic hardening and material anisotropy [6, 7]. For instance, in high-strength steels, out-of-phase torsional and axial loading with a 90° phase difference induces dislocation pile-ups and shear-driven slip band formation, accelerating fatigue damage [4, 8].

Early approaches to fatigue life prediction were grounded in classical theories [9]. Methods such as the local stress–strain [10], stress

https://doi.org/10.1002/msd2.70024

field intensity approach [11], critical plane method [6, 12, 13], energy-based approaches [14], and damage tolerance frameworks [2] formed the foundation of early research that retains its influence to this day. These models were later enhanced by incorporating multiaxial, nonproportional loading effects, and advanced numerical simulations [15–17]. In particular, the critical plane approach was adapted to account for nonproportional loading by introducing cyclic hardening models and stress path-dependent parameters [8]. Finite element-based simulations further enabled detailed evaluations of localized stress–strain responses, thereby improving the accuracy of predictions for complex geometries [18]. More recently, physics-informed neural networks also offer promising computational approaches for solving differential equations in mechanics [19]. While these developments have improved the ability to model multiaxial fatigue to a great extent, their reliance on simplifying assumptions, such as isotropic material behavior and parameter independence, limits their applicability to realistic and varying conditions. This gives rise to data-driven approaches capable of extrapolating patterns beyond parametric or semiparametric models [20–23].

Fatigue life is strongly influenced by environmental and operational factors. Elevated temperatures can accelerate crack propagation, as demonstrated in nickel-based superalloys under jet engine conditions, while marine environments exacerbate corrosion fatigue in structural steels [5]. The effects of loading path sensitivity have also been extensively studied, with approaches such as the critical plane method evaluating stress orientation and amplitude [6, 24]. Recent advancements include deep learning frameworks incorporating self-attention mechanisms to model the effects of loading history and temperature variations on multiaxial fatigue life [21], and studies examining load path sensitivity under nonproportional loading conditions [25], showing the necessity of their inclusion in fatigue life predictions. Despite this progress, the role of material property interactions, particularly under multiaxial and nonproportional loading, remains an underexplored area, warranting further investigation.

Material properties play an instrumental role in the fatigue resistance of metals. Elastic modulus (E), for instance, governs stiffness and stress redistribution, while yield strength (σ_y) defines the stress threshold at which plastic deformation begins [2]. Tensile strength (σ_t) is closely tied to fatigue strength, particularly in high-strength alloys, where fracture is the dominant failure mechanism [26]. Poisson's ratio (ν) affects lateral strain and shear stress redistribution [27]. However, these properties do not act independently; instead, they are often strongly correlated due to shared metallurgical processes, including alloying and heat treatment [4]. For instance, yield strength and tensile strength in structural steels often correlate strongly (coefficients > 0.85), reflecting shared microstructural attributes, like, grain size and dislocation density. In aluminum alloys, elastic modulus variations influence stress fields via interactions with Poisson's ratio, affecting crack propagation [27]. These interdependencies complicate efforts to isolate the individual effects of material properties on fatigue life, highlighting the need for integrated modeling approaches capable of addressing these correlations [28–30].

Sensitivity analysis (SA) aims to identify the influence of input parameters on model outputs. Variance-based global SA methods, such as those developed by Sobol [31] and refined by Saltelli et al. [32], have been widely applied in engineering for their ability to quantify both individual parameter effects and interactions. However, traditional SA methods assume parameter independence, which is often invalid in fatigue modeling where material properties exhibit strong correlations as described above. Neglecting parameter dependencies can lead to significant inaccuracies, as Vu-Bac et al. demonstrated in their modeling of Hi-Nicalon bundles, where accounting for correlations between stress and structural variations yielded more accurate fatigue predictions [28]. Similarly, their work on polymeric nanocomposites highlighted how capturing correlations among microstructural parameters strongly reinforces the reliability of mechanical property predictions [33]. Dependency-aware frameworks, such as those proposed by Kucherenko et al. [34] and Xu and Gertner [35], overcome these limitations by preserving the correlation structure of the inputs throughout the analysis. Alternative approaches like nonintrusive stochastic isogeometric analysis [36] have also addressed material uncertainty, though using continuity-preserving basis functions rather than our machine learning (ML) approach that may have an advantage in handling the irregular sampling and complex parameter dependencies present in multiaxial fatigue data. Additionally, Bayesian methodologies [37] provide probabilistic model assessment by updating prior knowledge, whereas our variance-based approach offers more direct quantification of input contributions, which is particularly advantageous when analyzing multiple correlated material properties under varied loading conditions.

The computational demands of fatigue life prediction further complicate sensitivity analyses. High-fidelity finite element analysis methods are often required to accurately simulate nonlinear behavior and multiaxial loading effects, but conducting the thousands of simulations needed for global SA is computationally prohibitive. Surrogate models, such as Random Forest (RF), Gaussian Processes, Artificial Neural Networks, and Extreme Gradient Boosting (XGBoost), provide an efficient alternative by approximating the behavior of high-fidelity models with high accuracy [38–42]. These models have been successfully applied in aerospace and mechanical systems to facilitate large-scale sensitivity studies and optimization [43–45]. In the context of fatigue modeling, surrogate models enable the integration of SA frameworks, particularly those addressing parameter correlations [28].

This study integrates ML-based surrogate models with dependency-aware SA to investigate the influence of material properties on multiaxial fatigue life. Using the data set collected by Chen et al. [26], which includes 1167 samples across 40 materials and 48 loading paths, we analyze the sensitivity of elastic modulus, yield strength, tensile strength, and Poisson's ratio to fatigue life. Surrogate models, including RF and XGBoost, are employed to approximate complex input–output relationships, enabling efficient sensitivity analyses. Dependency-aware SA frameworks, adapted from [34, 46], are used to capture the interdependencies among material properties, offering a deeper understanding of their combined effects on fatigue resistance.

The remainder of this paper is organized as follows. Section 2 describes the mechanical model and data set used in this study. Section 3 details the ML models and validation methods for surrogate modeling. Section 4 presents the SA framework, including dependency handling. Results and discussion are provided in Section 5, comparing model performances and sensitivity indices. Finally, Section 6 summarizes the findings and provides concluding remarks.

2 | Data Description

2.1 | Material Properties and Their Physical Significance

The mechanical properties of materials play a central role in fatigue performance under cyclic loading [3, 4]. Here, we assess four particularly influential properties: elastic modulus (X_1), tensile strength (X_2), yield strength (X_3), and Poisson's ratio (X_4). Each governs specific mechanisms underlying fatigue crack initiation, propagation, and failure, as detailed below.

Elastic modulus quantifies stiffness, controlling resistance to elastic deformation [3]. During high-cycle fatigue, where deformation is predominantly elastic, X_1 regulates strain energy storage and dissipation, which influences the stress distribution around defects. This behavior is described by

$$\sigma = E\varepsilon, \tag{1}$$

where σ is the applied stress, E is the elastic modulus, and ε is the elastic strain.

Figure 1A shows that materials in strain-controlled tests have higher X_1 values (clustered near 200 GPa), enabling them to endure significant cyclic strains. Conversely, stress-controlled tests focus on materials with $X_1 \sim 75$ GPa, reflecting their aptitude for elastic-dominated fatigue scenarios.

Tensile strength (X_2) measures the maximum stress a material withstands before failure and is critical for low-cycle fatigue involving substantial plastic deformation. The relationship between stress amplitude (σ_a) and fatigue life (N_f) is expressed by Basquin's law:

$$\sigma_a = \sigma_f'(2N_f)^b, \tag{2}$$

where σ_f' is the fatigue strength coefficient, and b the fatigue strength exponent [47].

Figure 1B demonstrates that strain-controlled tests cover a wider X_2 range, indicating the use of diverse materials under severe loading. In contrast, stress-controlled tests cluster near $X_2 \sim 600$MPa, indicative of materials optimized for elastic behavior.

Yield strength (X_3) defines the onset of plastic deformation. Cyclic loading near X_3 induces localized plasticity, forming persistent slip bands that often act as precursors to fatigue cracks [48]. The plastic stress–strain relationship can be represented as

$$\sigma = K'(\varepsilon_p)^n, \tag{3}$$

where K' is the cyclic strength coefficient, ε_p is the plastic strain, and n is the strain-hardening exponent.

As shown in Figure 2A, materials used in strain-controlled tests typically exhibit $X_3 > 1000$ MPa, enabling them to sustain significant plastic deformation. Conversely, stress-controlled tests involve materials with $X_3 \sim 500$ MPa, reflecting elastic-dominated conditions.

Poisson's ratio (X_4) characterizes the coupling between lateral and axial deformations. This property is particularly significant in multiaxial fatigue, where it dictates shear stress effects and crack propagation under nonproportional loading [4, 6]. The shear modulus (G) is related to X_4 by

$$G = \frac{E}{2(1+\nu)}, \tag{4}$$

where E is the elastic modulus, and ν is Poisson's ratio. Figure 2B shows that X_4 clusters near 0.3 for both test types, highlighting the prevalence of ductile materials in the data set.

The data set distinguishes between stress- and strain-controlled test regimes:

- *Stress-controlled tests:* Materials with lower X_1, X_2, and X_3 dominate, reflecting conditions suited for high-cycle fatigue with predominantly elastic deformation (Figures 1 and 2).

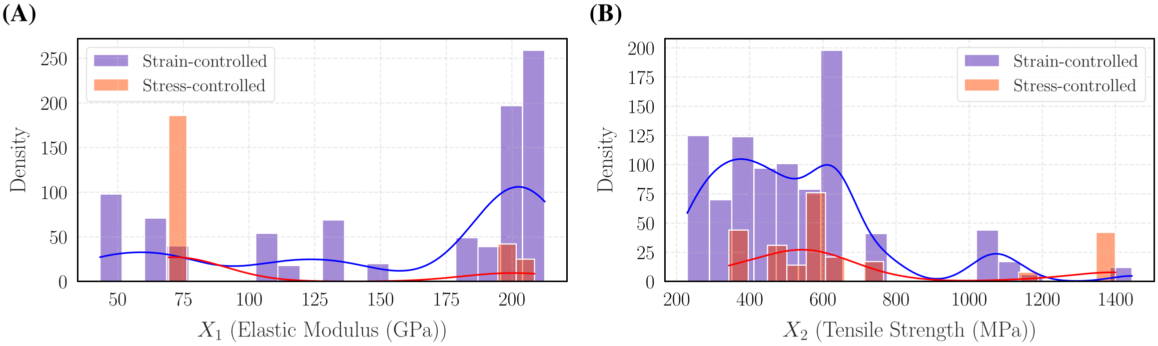

FIGURE 1 | Distributions of (A) elastic modulus and (B) tensile strength across stress- and strain-controlled tests.

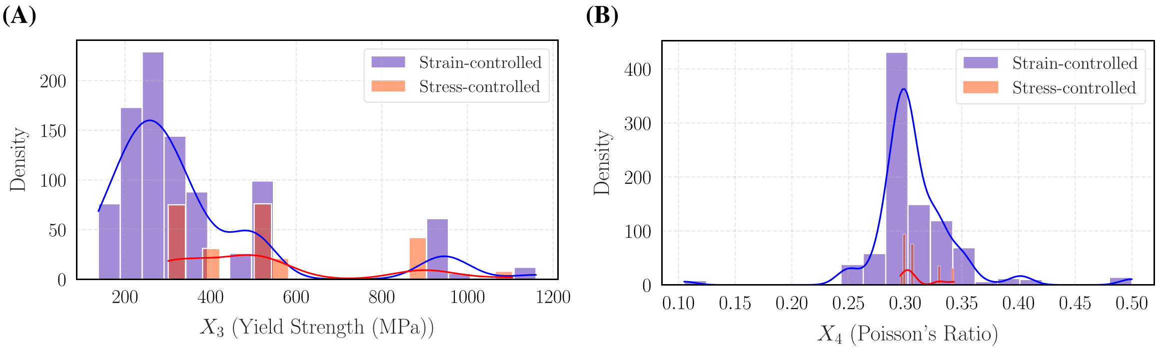

FIGURE 2 | Distributions of (A) yield strength and (B) Poisson's ratio across stress- and strain-controlled tests.

- *Strain-controlled tests:* Higher values of X_1, X_2, and X_3 characterize materials designed for low-cycle fatigue with significant plastic deformation (Figures 1 and 2).

Understanding the distributions of X_1X_4- (Figures 1 and 2) is conducive to generating representative samples and interpreting SA results (Section 5.2).

2.2 | Loading Path Characterization

Loading paths are fundamental to understanding fatigue behavior under cyclic loading as they directly influence stress distribution, crack initiation, and material response [6, 8, 25]. Here, each loading cycle in the data set is vectorized as a time series of 241 points, capturing the evolution of stress or strain components with high resolution. Stress-controlled tests are defined by axial stress $\sigma(t)$ and shear stress $\tau(t)$, while strain-controlled tests involve axial strain $\varepsilon(t)$ and shear strain $\gamma(t)$. This representation encodes critical features, such as amplitude, phase, and path geometry.

Three primary loading path classifications, uniaxial, proportional multiaxial, and nonproportional multiaxial, are included in the data set (Table 1):

- *Uniaxial paths:* Cyclic deformation occurs along a single axis, serving as a benchmark for evaluating fundamental fatigue mechanisms.
- *Proportional paths:* Axial and shear components maintain a fixed phase relationship, resulting in linear trajectories in stress or strain space. These paths are key for assessing materials under stable phase conditions.
- *Nonproportional paths:* Characterized by variable phase relationships, these paths produce complex trajectories (e.g., circular or elliptical). Subdivided into six types (I-VI), nonproportional paths induce principal stress rotations and activate additional hardening mechanisms [8, 17].

Nonproportional paths, in particular, represent the most demanding scenarios for fatigue modeling due to the intricacies of interaction between stress rotations and multiaxial damage mechanisms [15]. Principal stress rotations amplify cyclic hardening and significantly alter crack propagation trajectories. Their inclusion in the data set is necessary to maintain comprehensive coverage of multiaxial fatigue phenomena.

Surrogate models rely on high-quality input–output relationships to approximate computationally expensive simulations [38, 45]. By incorporating diverse and realistic loading conditions, the data set strengthens the ability of these models to capture the nuances of fatigue behavior across varied stress states.

Table 1 illustrates the representative patterns of each classification, providing insights into the underlying stress or strain trajectories. This diversity in loading paths demonstrates the robustness and expansiveness of the data set, crucial for accurate surrogate model development.

Note that loading paths are visualized in the stress/strain space, where the horizontal axis represents axial stress/strain, and the vertical axis represents shear stress/strain. Each path represents one complete loading cycle, encapsulating the trajectory of multiaxial deformation.

2.3 | Data Set Description and Statistical Information

The data set used in this study contains 1167 multiaxial fatigue test samples from 40 different metallic materials, including stainless steels, aluminum alloys, titanium alloys, and nickel-based superalloys [26]. These samples cover 48 distinct multiaxial loading paths and include both stress- and strain-controlled conditions. This data set provides a comprehensive foundation for studying the mechanical and fatigue properties of metals under various conditions.

The data set's construction involved an extensive literature review, with 36 studies selected from over 70 sources. Selection criteria emphasized high-quality experimental data and complete reporting of material properties and loading conditions. Most tests were conducted at room temperature, with the exception of GH4169 and Hayes alloys, which underwent high-temperature testing [26].

Figure 3 shows the correlations among the four mechanical properties in consideration: elastic modulus (X_1), tensile strength (X_2), yield strength (X_3), and Poisson's ratio (X_4). Tensile strength and yield strength (X_2 and X_3) are strongly correlated ($r = 0.89$), reflecting their shared dependence on material composition and processing, such as heat treatment and alloying. These properties play a key role in fatigue

TABLE 1 | Loading path classifications and representative patterns.

Loading paths	Plots
Uniaxial	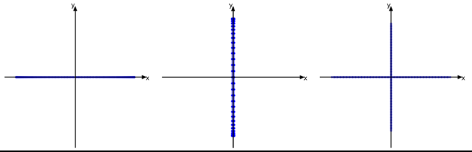
Proportional	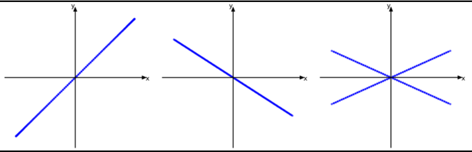
Non-proportional I	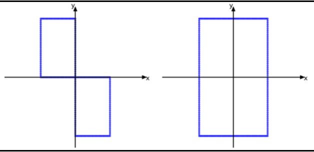
Non-proportional II	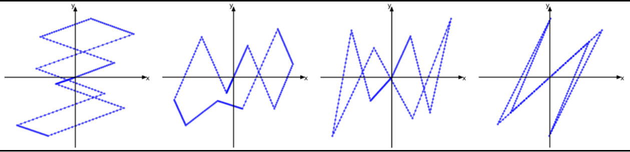
Non-proportional III	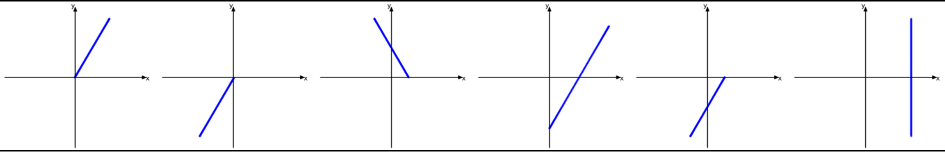
Non-proportional IV	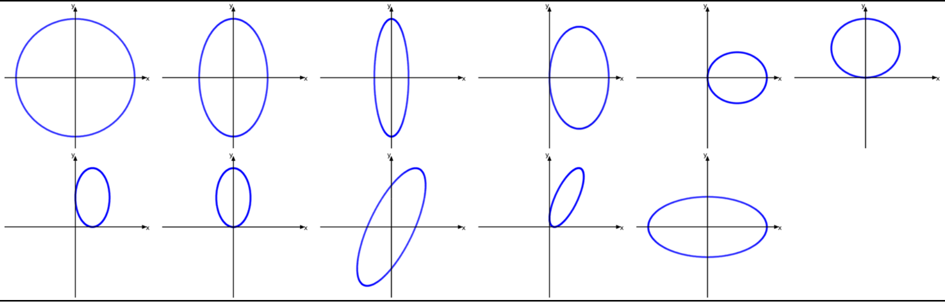
Non-proportional V	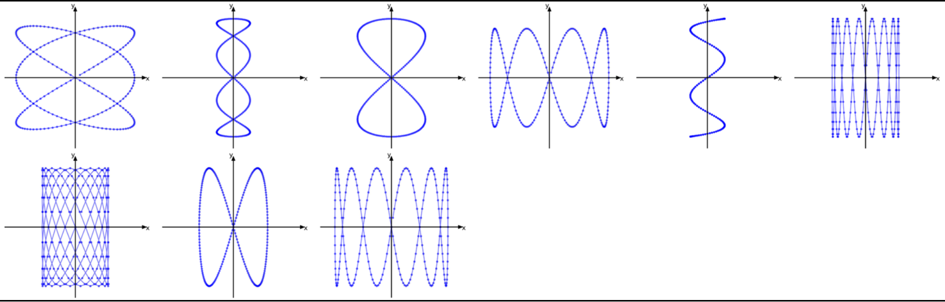
Non-proportional VI	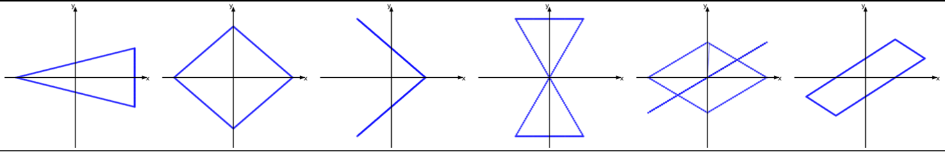

resistance, particularly in controlling plastic deformation and delaying crack initiation [49].

Elastic modulus (X_1) and Poisson's ratio (X_4) exhibit weaker correlations with other properties and with each other. This suggests that they contribute to fatigue behavior independently. Elastic modulus governs stress distribution and elastic deformation, while Poisson's ratio affects how materials deform laterally under axial loading. These distinct roles will be further illuminated through SA results.

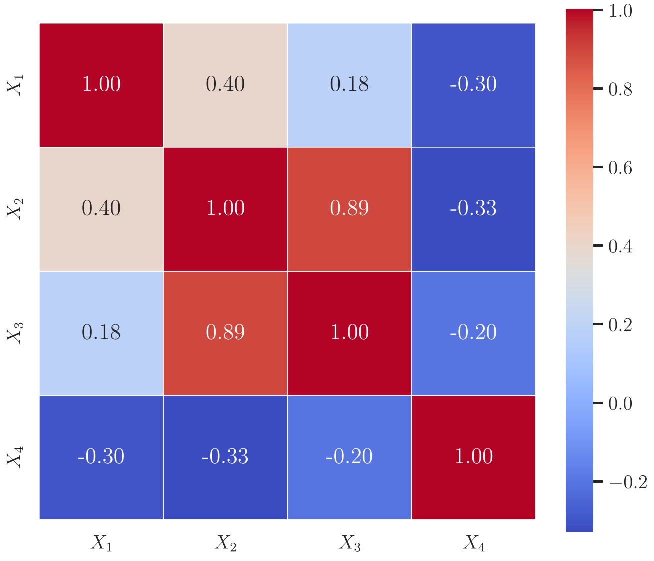

FIGURE 3 | Correlation matrix among material properties: X_1, X_2, X_3, and X_4.

Figure 4 illustrates the distributions and pairwise relationships among X_1, X_2, X_3, and X_4, separated by stress- and strain-controlled test conditions. Materials used in strain-controlled tests generally have higher tensile strength (X_2) and yield strength (X_3), allowing them to endure significant plastic deformation during low-cycle fatigue. In contrast, stress-controlled tests focus on materials with lower elastic modulus (X_1), which are better suited for high-cycle fatigue where elastic deformation dominates.

3 | Surrogate Models for Fatigue Life Prediction

In this study, we use RF and XGBoost as surrogate models to predict fatigue life ($\log(N_f)$) under multiaxial loading. Both models are capable of capturing complex, nonlinear interactions among mechanical properties while providing computational efficiency that makes them advantageous over traditional physics-based simulations [50–52]. Their formulations are detailed below.

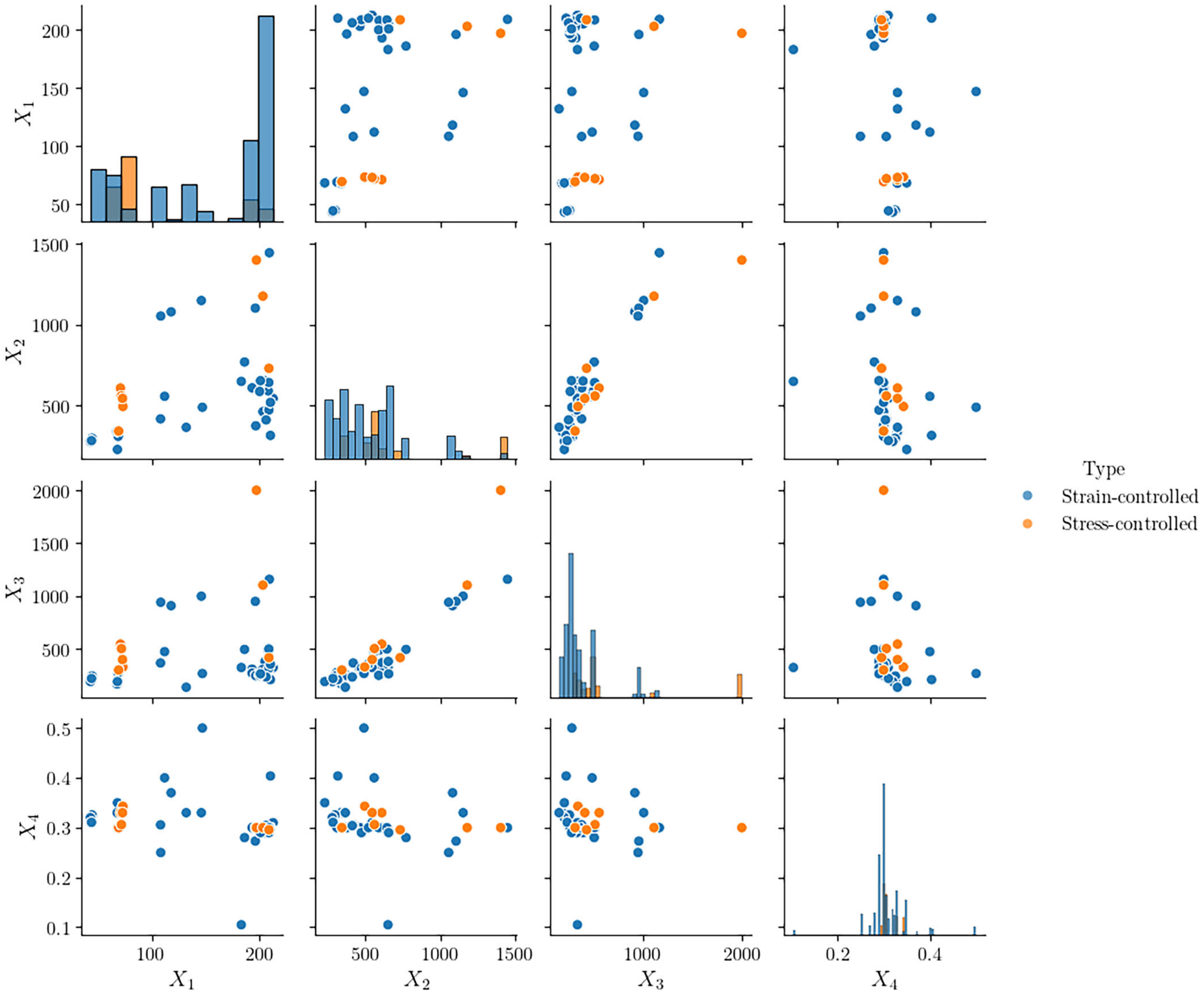

FIGURE 4 | Scatter plot matrix showing distributions and pairwise relationships among X_1, X_2, X_3, and X_4, separated by test type.

3.1 | Random Forest

RF is an ensemble learning algorithm that constructs N_t decision trees using randomly bootstrapped subsets of the data set [50]. Each tree is built recursively, splitting the feature space to minimize impurity. For regression tasks, impurity is minimized by selecting the feature X_j and threshold s at each node that solves

$$\underset{j,s}{\operatorname{argmin}} \left[\frac{N_{\mathrm{L}}}{N} \cdot \operatorname{Var}(Y_{\mathrm{L}}) + \frac{N_{\mathrm{R}}}{N} \cdot \operatorname{Var}(Y_{\mathrm{R}})\right], \tag{5}$$

where N_{L} and N_{R} are the number of samples in the left (Y_{L}) and right (Y_{R}) child nodes, respectively, and $\operatorname{Var}(Y)$ represents the variance of the target values Y in a given node.

The prediction from a single tree is denoted as $f_i(X)$, where i is the tree index. The final RF prediction aggregates the outputs from all N_t trees:

$$\hat{y} = \frac{1}{N_t}\sum_{i=1}^{N_t} f_i(X). \tag{6}$$

RF's ability to model nonlinear interactions and rank features by their contribution to variance reduction makes it an appropriate tool for fatigue life prediction [42].

3.2 | Extreme Gradient Boosting

XGBoost builds an ensemble of trees sequentially, where each tree $h_t(X)$ corrects the residual errors of the previous iteration [51]. The model at iteration t is given by

$$\hat{y}_t = \hat{y}_{t-1} + \eta \cdot h_t(X), \tag{7}$$

where η is the learning rate, and $h_t(X)$ represents the tree added at iteration t.

XGBoost optimizes a regularized objective function:

$$L = \sum_{i=1}^{n} l(y_i, \hat{y}_i) + \sum_{t=1}^{T} \Omega(h_t), \tag{8}$$

where $l(y_i, \hat{y}_i)$ is the loss function (e.g., squared error for regression tasks), and $\Omega(h_t)$ is the regularization term which controls model complexity, and is defined as

$$\Omega(h_t) = \gamma T + \frac{\lambda}{2}\sum_{j=1}^{T} w_j^2, \tag{9}$$

where T is the number of leaves in the tree, w_j represents the weight of leaf j, γ penalizes the number of leaves, and λ penalizes large weights to control overfitting.

At each iteration, XGBoost employs a second-order Taylor approximation of the loss function:

$$L^{(t)} \approx \sum_{i=1}^{n}\left[g_i h_t(X_i) + \frac{1}{2} h_i h_t(X_i)^2\right] + \Omega(h_t), \tag{10}$$

where $g_i = \frac{\partial l(y_i, \hat{y}_{t-1})}{\partial \hat{y}_{t-1}}$ and $h_i = \frac{\partial^2 l(y_i, \hat{y}_{t-1})}{\partial \hat{y}_{t-1}^2}$ are the first and second derivatives of the loss function with respect to the previous prediction $\hat{y}_{t-1}$.

The optimal weights w_j for each leaf in the tree are computed analytically by minimizing $L^{(t)}$:

$$w_j = -\frac{\sum_{i \in I_j} g_i}{\sum_{i \in I_j} h_i + \lambda}, \tag{11}$$

where I_j is the set of samples assigned to leaf j. This gradient-based refinement allows XGBoost to iteratively improve predictions and spot intricate patterns in data.

3.3 | Model Training and Hyperparameter Optimization Process

Both RF and XGBoost models were trained using mechanical properties (X_1, X_2, X_3, X_4) as inputs, with fatigue life ($\log(N_{\mathrm{f}})$) as the target. Preprocessing included log transformation of the target variable for normalization, standardization of features for consistent scaling. Data set partitioning into training (70%), validation (15%), and testing (15%) subsets was done to achieve robust and generalizable models. Additionally, hyperparameter optimization was performed using a combination of heuristic methods and grid search.

For RF, key hyperparameters included the number of trees (N_t), features per split (m), and minimum samples per leaf. Grid search across $100 \leq N_t \leq 1000$ (in increments of 100) showed optimal performance at $N_t = 500$. Features per split were set to $m = \sqrt{p}$, and min_samples_leaf = 2 was selected to balance complexity and variance reduction.

For XGBoost, the learning rate (η), maximum depth (d), L_2 regularization (λ), and subsampling ratio were optimized. Coarse grid search and fine-tuning identified $\eta = 0.01, d = 6, \lambda = 1$, and subsample= 0.8 as the best configuration. Early stopping was employed, terminating training when validation performance did not improve for 20 iterations.

3.4 | Performance Metrics

Model performance was evaluated on the test set using the following metrics:

$$R^2 = 1 - \frac{\sum_{i=1}^{n}(y_i - \hat{y}_i)^2}{\sum_{i=1}^{n}(y_i - \bar{y})^2}, \quad \mathrm{RMSE} = \sqrt{\frac{1}{n}\sum_{i=1}^{n}(y_i - \hat{y}_i)^2},$$

$$\mathrm{MAE} = \frac{1}{n}\sum_{i=1}^{n}|y_i - \hat{y}_i|, \quad \mathrm{RD} = \frac{1}{n}\sum_{i=1}^{n}\frac{|y_i - \hat{y}_i|}{y_i}.$$

Here, R^2 quantifies the proportion of variance explained by the model ($R^2 > 0.8$ is set as the minimum threshold for acceptable accuracy) [46]. Root mean squared error (RMSE) and mean absolute error (MAE) capture the average prediction error, while relative deviation (RD) provides a scale-independent measure of deviation.

A potential point of contention that should be addressed is the use of more traditional ML models (RF and XGBoost) over demonstrably excellent deep learning models, such as long short-term memory and gated recurrent unit [26]. However, their deployment as surrogate models in this study poses several practical challenges. First, deep learning models typically require substantial computational resources for training and inference, making them less suitable for rapid SA, where model evaluations are performed thousands of times. In contrast, RF and XGBoost offer comparable performance with significantly reduced computational overhead during both training and prediction. Second, the relatively small size of the data set (1167 samples) limits the advantage deep learning might provide, as such models are inherently data-hungry and prone to overfitting when the training data is scarce. RF and XGBoost are robust to smaller data sets, effectively leveraging their ensemble architectures to prevent overfitting. Finally, the interpretability of RF and XGBoost, through feature importance and SHAP values, aligns well with the objectives of SA, which require clear insight into input–output relationships. These considerations collectively make RF and XGBoost more efficient and practical choices for this study.

These surrogate models make it possible to quickly assess fatigue life across diverse conditions, facilitating not global SA, but also optimization tasks, and uncertainty quantification [43, 44], thereby bridging the gap between computational and experimental fatigue studies.

4 | SA Framework for Dependent Variables

This section presents the SA framework tailored for fatigue life prediction models with dependent input variables. Following methodologies from [30, 34, 53, 54], the approach adapts traditional Sobol's indices to account for input correlations, enabling a more accurate quantification of variance contributions.

4.1 | Incorporating Input Dependencies

Material properties in fatigue life modeling exhibit significant correlations, as demonstrated in Section 2.1. Ignoring these dependencies can yield misleading sensitivity indices. To address this, the following steps incorporate these dependencies directly into the SA framework.

First, the correlation matrix $\boldsymbol{\Sigma}$ is derived from the empirical data set, encapsulating the relationships among the input variables:

$$\boldsymbol{\Sigma} = \begin{bmatrix} 1 & 0.40 & 0.18 & -0.30 \\ 0.40 & 1 & 0.89 & -0.33 \\ 0.18 & 0.89 & 1 & -0.20 \\ -0.30 & -0.33 & -0.20 & 1 \end{bmatrix}, \tag{12}$$

where each element ρ_{ij} denotes the Pearson correlation coefficient between X_i and X_j:

$$\rho_{ij} = \frac{\mathrm{Cov}(X_i, X_j)}{\sqrt{\mathrm{Var}(X_i)\mathrm{Var}(X_j)}}. \tag{13}$$

This matrix reflects the empirical relationships between material properties, ensuring that the input space retains realistic correlations.

The correlation matrix $\boldsymbol{\Sigma}$ must be symmetric and positive definite for mathematical operations, including variance decomposition and Sobol's sensitivity index computation. If numerical errors render $\boldsymbol{\Sigma}$ nonpositive definite, it is corrected using the nearest positive definite matrix algorithm [34]:

$$\boldsymbol{\Sigma}_{\text{new}} = \boldsymbol{\Sigma}_{\text{original}} + \epsilon \boldsymbol{I}, \tag{14}$$

where $\boldsymbol{I}$ is the identity matrix, and $\epsilon > 0$ is a small constant ensuring positive definiteness.

Once the matrix $\boldsymbol{\Sigma}$ is validated as positive definite, Cholesky decomposition is applied:

$$\boldsymbol{\Sigma} = \boldsymbol{L}\boldsymbol{L}^{\mathrm{T}}, \tag{15}$$

where $\boldsymbol{L}$ is a lower triangular matrix. The elements of $\boldsymbol{L}$ are computed as

$$L_{ij} = \begin{cases} \sqrt{\Sigma_{ii} - \sum_{k=1}^{i-1} L_{ik}^2} & \text{if } i = j, \\ \frac{\Sigma_{ij} - \sum_{k=1}^{i-1} L_{ik}L_{jk}}{L_{ii}} & \text{if } i \neq j. \end{cases} \tag{16}$$

This decomposition facilitates stable numerical operations required for SA.

Unlike synthetic sampling approaches, such as Latin Hypercube Sampling, this method directly uses the empirical data set. Material properties and their inherent correlations are preserved without transformation into standard normal space. This ensures that the SA reflects the actual experimental data.

4.2 | Variance Decomposition Using ANOVA

The variance decomposition of the output $Y = f(\boldsymbol{X})$ serves as the foundation for SA. The total variance $V(Y)$ is partitioned into contributions from individual inputs and their interactions. For n input variables $\boldsymbol{X} = [X_1, X_2, \ldots, X_n]^{\mathrm{T}}$, the function $f(\boldsymbol{X})$ is expressed as

$$f(\boldsymbol{X}) = f_0 + \sum_{i=1}^{n} f_i(\boldsymbol{X}_i) + \sum_{i<j} f_{ij}(\boldsymbol{X}_i, \boldsymbol{X}_j) + \cdots, \tag{17}$$

where

- $f_0 = \mathbb{E}[f(\boldsymbol{X})]$ is the mean value of f,
- $f_i(\boldsymbol{X}_i)$ is the first-order contribution of $\boldsymbol{X}_i$,
- $f_{ij}(\boldsymbol{X}_i, \boldsymbol{X}_j)$ represents the interaction between $\boldsymbol{X}_i$ and $\boldsymbol{X}_j$, and so on.

This decomposition is grounded in the principles of ANOVA, as detailed in [53, 54], and maintains orthogonality, such that:

$$\mathbb{E}\left[f_i(\boldsymbol{X}_i) \cdot f_j(\boldsymbol{X}_j)\right] = 0 \quad \text{for } i \neq j. \tag{18}$$

The total variance $V(Y)$ is then decomposed as

$$V(Y) = \mathrm{Var}[f(\boldsymbol{X})] = \sum_{i=1}^{n} V_i + \sum_{i<j} V_{ij} + \cdots, \tag{19}$$

where

- $V_i = \mathrm{Var}[f_i(\boldsymbol{X}_i)]$ is the first-order contribution of $\boldsymbol{X}_i$,
- $V_{ij} = \mathrm{Var}[f_{ij}(\boldsymbol{X}_i, \boldsymbol{X}_j)]$ is the interaction variance between $\boldsymbol{X}_i$ and $\boldsymbol{X}_j$.

The total variance $V(Y)$ is the sum of these contributions:

$$\sum_{i=1}^{n} V_i + \sum_{i<j} V_{ij} + \cdots + V_{12\ldots n} = V(Y). \tag{20}$$

4.3 | Sobol's Sensitivity Indices

Sobol's indices quantify the contributions of inputs and their interactions to the total variance [34]:

- The first-order Sobol's index S_i:

  $$S_i = \frac{V_i}{V(Y)} = \frac{\mathrm{Var}[\mathbb{E}[Y|\boldsymbol{X}_i]]}{\mathrm{Var}(Y)} \tag{21}$$

  measures the contribution of $\boldsymbol{X}_i$ alone.

- The total-effect Sobol's index $S_{T(i)}$:

  $$S_{T(i)} = 1 - \frac{\mathrm{Var}[Y|\boldsymbol{X}_i]}{\mathrm{Var}(Y)} \tag{22}$$

  represents the overall contribution of $\boldsymbol{X}_i$, including higher-order interactions.

- The second-order Sobol's index S_{ij}:

  $$S_{ij} = \frac{V_{ij}}{V(Y)} = \frac{\mathrm{Var}[\mathbb{E}[Y|\boldsymbol{X}_i, \boldsymbol{X}_j]] - V_i - V_j}{\mathrm{Var}(Y)}, \tag{23}$$

  quantifies the interaction effect between $\boldsymbol{X}_i$ and $\boldsymbol{X}_j$.

4.4 | Monte Carlo (MC) Estimation of Sobol's Indices

MC integration is used to estimate Sobol's indices by systematically sampling the input space and evaluating variance contributions [46, 53]. For a given model $f(\boldsymbol{X})$, two sample sets are required:

1. *Baseline samples* ($\boldsymbol{X}_A$): Independently generated input samples.
2. *Perturbed samples* ($\boldsymbol{X}_{AB}$): Constructed by replacing the ith column of $\boldsymbol{X}_A$ with the corresponding column from another set $\boldsymbol{X}_B$:

$$\boldsymbol{X}_{AB} = \left[\boldsymbol{X}_1^A, \boldsymbol{X}_2^A, \ldots, \boldsymbol{X}_i^B, \ldots, \boldsymbol{X}_n^A\right]. \tag{24}$$

The first-order index S_i, representing the contribution of X_i to the total variance, is approximated as

$$S_i \approx \frac{\frac{1}{N}\sum_{k=1}^{N} f\left(\boldsymbol{X}_A^{(k)}\right) f\left(\boldsymbol{X}_{AB}^{(k)}\right) - \left(\frac{1}{N}\sum_{k=1}^{N} f\left(\boldsymbol{X}_A^{(k)}\right)\right)^2}{\mathrm{Var}(f(\boldsymbol{X}))}, \tag{25}$$

where

- $f(\boldsymbol{X}_A^{(k)})$: Model output for the kth baseline sample.
- $f(\boldsymbol{X}_{AB}^{(k)})$: Model output for the kth perturbed sample.
- $\mathrm{Var}(f(\boldsymbol{X}))$: Total variance over the baseline samples.

The total-effect index S_{T_i}, which captures the combined contribution of X_i and all its interactions, is estimated as

$$S_{T_i} \approx \frac{\frac{1}{N}\sum_{k=1}^{N}\left(f\left(\boldsymbol{X}_A^{(k)}\right) - f\left(\boldsymbol{X}_{AB}^{(k)}\right)\right)^2}{2 \cdot \mathrm{Var}(f(\boldsymbol{X}))}. \tag{26}$$

The numerator quantifies variance induced by perturbations of $\boldsymbol{X}_i$, isolating its total effect.

4.5 | Integration With Surrogate Models

Given the computational cost of high-fidelity models, a surrogate model $f_{\text{surrogate}}$ (e.g., XGBoost) is trained to approximate $f(\boldsymbol{X})$ (see Section 3). The surrogate's performance is validated using metrics, such as R^2, RMSE, and MAE. Once validated, the surrogate replaces the computationally expensive model for efficient computation of sensitivity indices [30].

This framework ensures that the correlations among material properties are accounted for, improving the physical interpretability of the sensitivity indices. The quantified indices in subsequent sections will illustrate how these correlations influence fatigue life predictions via both direct contributions and interaction effects.

4.6 | Implementation Procedure

Below is a streamlined summary of the SA workflow, consolidating the detailed steps previously outlined for clarity and reference, for more details see [34, 46, 53, 54].

Step 1: Data set preparation and analysis

- Utilize the existing data set containing fatigue life and mechanical properties.
- Extract relevant variables, ensuring input–output consistency.

$$\{\text{Original Dataset}\} \xrightarrow{\text{Extraction}} \{\boldsymbol{X}, \boldsymbol{y}\}.$$

Step 2: Transforming dependent inputs

- Extract the correlation matrix $\boldsymbol{\Sigma}$ directly from the data set.
- Validate the positive definiteness of $\boldsymbol{\Sigma}$ using Cholesky decomposition.
- Ensure transformed samples align with the dependent input structure.

$$\left\{\boldsymbol{X}_{\text{original}}\right\} \xrightarrow{\text{Cholesky Validation}} \left\{\boldsymbol{X}_{\text{dependent}}\right\}.$$

Step 3: Surrogate model construction and validation

- Partition the data set into training and testing subsets.
- Train a surrogate model, for example, XGBoost, to approximate $f(\boldsymbol{X})$.
- Validate the surrogate model using metrics, such as R^2, RMSE, and MAE.

$$\{\boldsymbol{X}_{\text{dependent}}, f(\boldsymbol{X})\} \xrightarrow{\text{Surrogate Model}} \{f_{\text{surrogate}}\}$$

Step 4: Variance decomposition using ANOVA

- Partition the surrogate model output variance $V(f_{\text{surrogate}}(\boldsymbol{X}))$ into contributions.
- Compute orthogonal components:

$$V(f_{\text{surrogate}}(\boldsymbol{X})) = \sum_i V_i + \sum_{i<j} V_{ij} + \cdots.$$

First-order variance $V_i = \mathrm{Var}[\mathbb{E}(f_{\text{surrogate}}(\boldsymbol{X})|X_i)]$. Interaction variance $V_{ij} = \mathrm{Var}[\mathbb{E}(f_{\text{surrogate}}(\boldsymbol{X})|X_i, X_j)] - V_i - V_j$.

Step 5: MC estimation of sensitivity indices

- Apply MC sampling to compute Sobol's indices: $S_i = \frac{V_i}{V(f_{\text{surrogate}}(\boldsymbol{X}))}$.
- Compute total-effect indices: $S_{T,i} = 1 - \frac{\mathrm{Var}(f_{\text{surrogate}}(\boldsymbol{X}) \mid X_i)}{V(f_{\text{surrogate}}(\boldsymbol{X}))}$.
- Use dependent input samples to estimate higher-order indices.

$$\left\{f_{\text{surrogate}}\right\} \xrightarrow{\text{MC Estimation}} \left\{S_i, S_{T,i}, S_{ij}\right\}.$$

This workflow integrates the data set's inherent dependency structure, reduces computational costs through surrogate modeling, and ensures reliable computation of sensitivity indices. Each step builds sequentially, emphasizing accuracy and efficiency.

5 | Results and Discussion

5.1 | Performance of Surrogate Models

Both surrogate models demonstrated strong predictive capabilities for fatigue life estimation, with XGBoost showing slightly better performance across all evaluation metrics (Table 2). The XGBoost model achieved an R^2 of 0.9258 and RMSE of 0.2006, compared with RF's R^2 of 0.8973 and RMSE of 0.2355. The relative difference of 4.11% for XGBoost indicates excellent prediction accuracy across the range of fatigue life values.

The parity plots (Figure 5) illustrate consistent performance between the training and test sets, with most predictions except one falling within the factor of 1.5 scatter bands. Both models maintain good accuracy across the fatigue life range, though slightly higher scatter is observed at extreme values. The XGBoost model's superior performance can be attributed to its gradient boosting architecture and regularization techniques making use of second-order derivatives to capture nonlinear relationship in fatigue life prediction.

The achieved performance metrics indicate that both surrogate models can serve as reliable replacements for computationally expensive finite element simulations in subsequent sensitivity analyses. However, the XGBoost model, with its higher accuracy and lower prediction errors, was selected as the primary surrogate model.

5.2 | Sensitivity Analysis

The SA quantifies the influence of material properties (X_1, X_2, X_3, X_4) on the variability of fatigue life predictions, while incorporating dependencies among inputs. This approach provides a more nuanced and physically grounded understanding of how material characteristics contribute to fatigue performance under multiaxial loading. Figures 6 and 7 present the first-order $(\hat{S}_1)$ and total-effect $(\hat{S}_T)$ sensitivity indices for dependent and independent inputs, respectively.

TABLE 2 | Performance metrics of Random Forest and XGBoost models.

Metric	Random forest	XGBoost
R^2	0.8973	0.9258
MSE	0.0641	0.0463
RMSE	0.2355	0.2006
MAE	0.1754	0.1491
RD (%)	4.8829	4.1124

Abbreviation: RD, relative deviation.

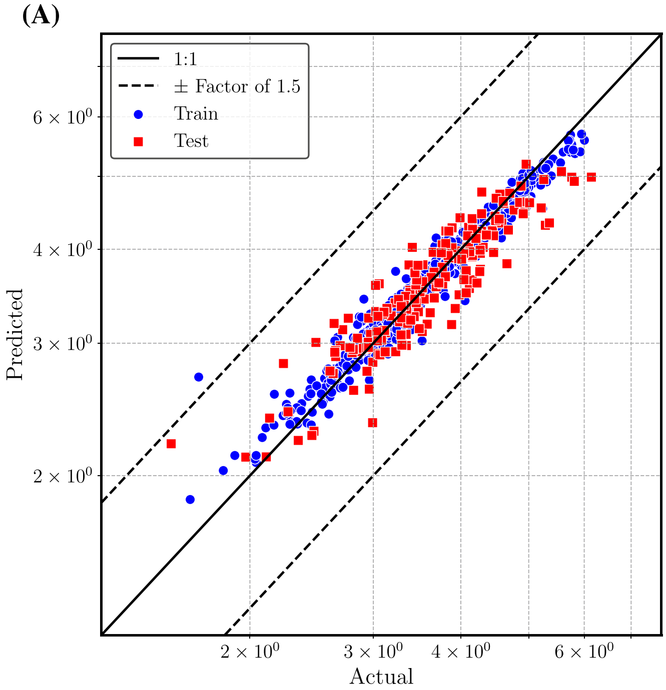

FIGURE 5 | Predicted versus actual fatigue life on logarithmic scale for (A) Random Forest and (B) XGBoost. Solid line represents the perfect prediction (1:1), dashed lines indicate factor of 1.5 scatter bands. Blue circles represent training data, red squares represent test data.

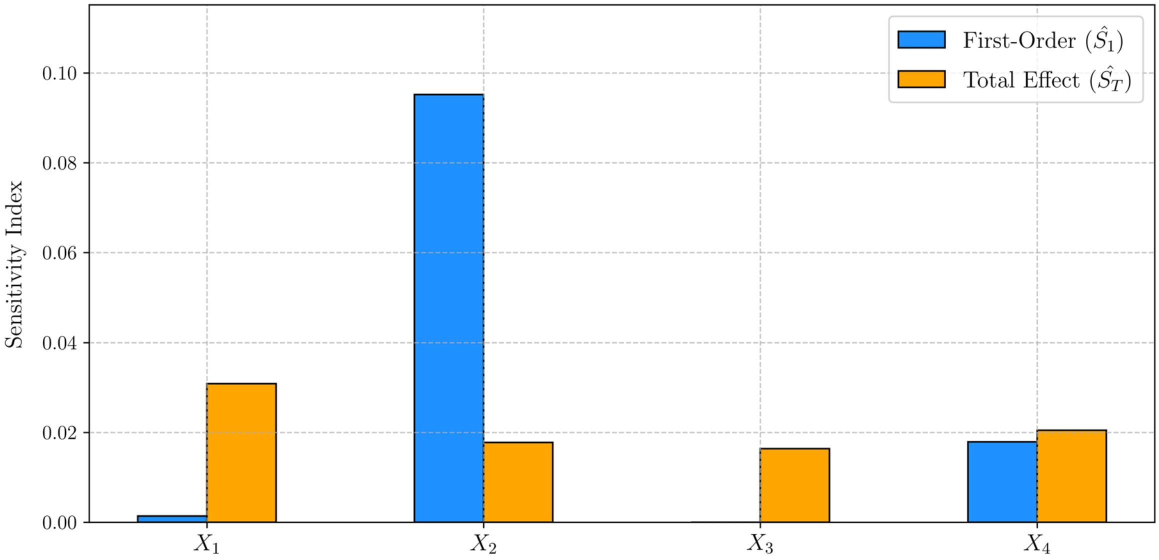

FIGURE 6 | First-order ($\hat{S}_1$) and total-effect ($\hat{S}_T$) sensitivity indices for dependent inputs.

5.2.1 | Dominant Parameter Influence

The analysis reveals that X_2 (tensile strength) is the dominant parameter influencing fatigue life, with the highest first-order sensitivity index ($\hat{S}_1 = 0.0952$) in the dependent case. Tensile strength directly controls a material's ability to resist cyclic loading by influencing both crack initiation and propagation phases. High tensile strength materials can sustain larger stress amplitudes before failure, which explains X_2's significant impact on fatigue life variability. This result is consistent with prior findings that link tensile strength to fatigue resistance across various metallic materials [6, 8].

Interestingly, X_1 (elastic modulus), which governs stiffness and stress redistribution, exhibits negligible first-order sensitivity ($\hat{S}_1 = 0.0014$) in the dependent case. This observation highlights the interplay between stiffness and other properties, such as X_2 and X_3, which overshadow the isolated effect of X_1. While elastic modulus influences local stress fields and energy storage during loading, its contribution to fatigue life variability is minimal when considered independently.

5.2.2 | Interaction Effects

The results highlight the importance of parameter interactions, particularly second-order effects, in determining fatigue life. As shown in Figure 8, the interaction between X_2 (tensile

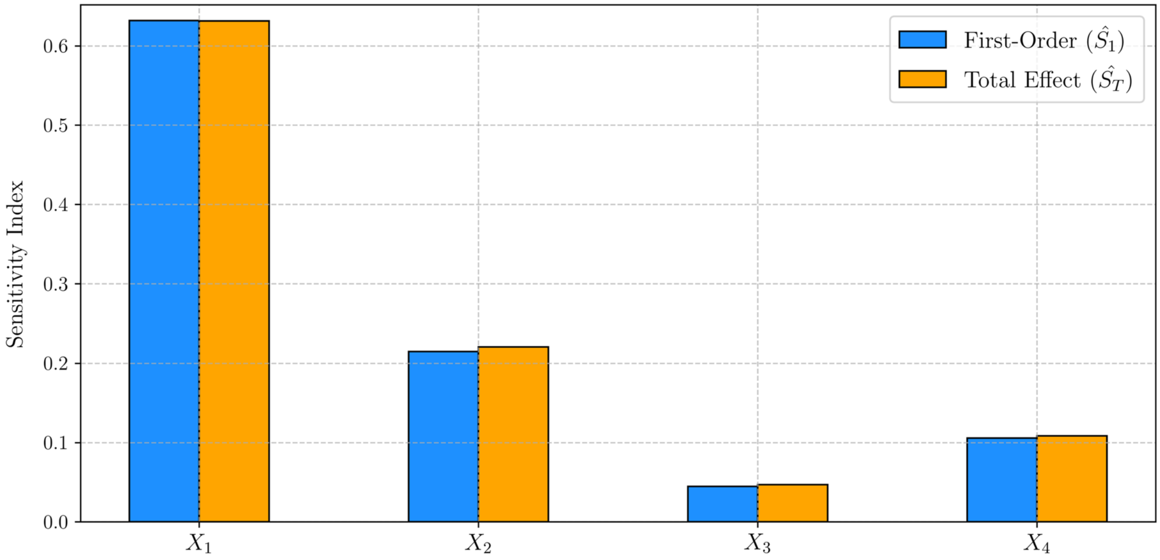

FIGURE 7 | First-order ($\hat{S}_1$) and total-effect ($\hat{S}_T$) sensitivity indices for independent inputs.

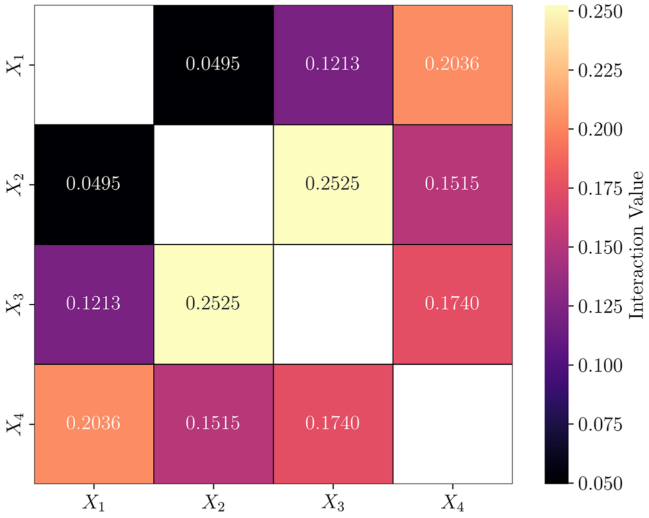

FIGURE 8 | Heatmap of second-order sensitivity interactions for dependent inputs.

strength) and X_3 (yield strength) is the most significant ($\hat{S}_{ij} = 0.2525$). This interaction reflects the synergistic role of these properties in controlling plastic deformation mechanisms and crack growth. Tensile strength sets the material's resistance to cyclic stresses, while yield strength determines the stress threshold for plastic deformation. Together, they govern the material's response to multiaxial loading, particularly under conditions involving significant strain localization [1].

Another notable interaction involves X_1 (elastic modulus) and X_4 (strain-hardening exponent) ($\hat{S}_{ij} = 0.2036$). This combination influences stress redistribution and energy dissipation during cyclic loading. Strain hardening enhances the material's ability to resist localized plasticity, while elastic modulus dictates the stiffness of the surrounding matrix. Their interaction directly affects the redistribution of stress near cracks or defects.

5.2.3 | Comparison With Independent Inputs

To evaluate the impact of accounting for input dependencies, sensitivity indices were computed for both dependent and independent cases. Figure 7 and Table 3 highlight the significant differences in the results. In the independent case, X_1 (elastic modulus) is incorrectly identified as the most influential parameter ($\hat{S}_1 = 0.6318$). This misrepresentation arises from neglecting the correlations among material properties, which artificially inflates the isolated contribution of X_1. Physically, stiffness primarily moderates stress distributions and does not directly drive fatigue life variability [2].

Conversely, the dependent case correctly identifies X_2 (tensile strength) as the dominant factor. The total-effect index for X_3 (yield strength) and X_4 (strain-hardening exponent) also decreases in the dependent case, reflecting their reduced individual contributions once correlations with X_2 are accounted for. This underscores the importance of accounting for input dependencies to achieve accurate and physically consistent SA [34, 46].

The findings here provide the following key insights:

- The dominant influence of X_2 aligns with its established role in fatigue resistance, emphasizing the need for precise tensile strength characterization in fatigue modeling.
- Strong second-order interactions, particularly between X_2 and X_3, highlight the importance of considering coupled effects rather than isolating individual parameters.
- Ignoring input dependencies leads to misleading conclusions, as demonstrated by the overestimated influence of X_1 in the independent case. This reinforces the need for dependency-aware methodologies in SA.

By accounting for correlated inputs, this analysis enhances the physical interpretability of sensitivity indices and provides a more reliable foundation for fatigue life predictions in multiaxial loading scenarios.

TABLE 3 | Comparison of sensitivity indices for dependent and independent inputs.

	First order ($\hat{S}_1$)		Total effect ($\hat{S}_T$)	
Parameter	**Dependent**	**Independent**	**Dependent**	**Independent**
X_1	0.0014	0.6318	0.0309	0.6314
X_2	0.0952	0.2149	0.0178	0.2205
X_3	0.0000	0.0448	0.0164	0.0469
X_4	0.0179	0.1058	0.0205	0.1084

6 | Conclusions

A framework for multiaxial fatigue life assessment for metallic components was developed by combining ML-based surrogate models with SA accounting for dependent inputs. The main findings include:

- The XGBoost model achieved the highest predictive accuracy ($R^2 = 0.9258$, $\mathrm{RMSE} = 0.2006$), demonstrating its effectiveness in modeling the nonlinear relationships inherent in multiaxial fatigue data. Thus, it was considered sufficient as a surrogate model.
- Tensile strength (X_2) was identified as the most influential parameter, with the highest first-order sensitivity index. Its critical role in fatigue life prediction is consistent with its established effect on cyclic stress resistance.
- Second-order interactions, especially between tensile strength (X_2) and yield strength (X_3), were significant, reflecting the interdependence of material properties in fatigue mechanisms.
- Comparing dependent and independent input scenarios revealed that ignoring parameter correlations distorts sensitivity indices, overestimating the influence of properties, like, elastic modulus (X_1).

These insights highlight the integral role of incorporating dependency-aware SA to achieve reliable and physically interpretable results in fatigue modeling. Future work can extend this framework to include additional factors such as microstructural effects or environmental influences for broader applicability.

Acknowledgments

We acknowledge Ho Chi Minh City University of Technology (HCMUT), VNU-HCM for supporting this study.

Conflicts of Interest

The authors declare no conflicts of interest.

Data Availability Statement

The data that support the findings of this study are openly available in Scientific Data at https://doi.org/10.1038/s41597-024-03862-4, reference number [26].

References

1. H. Mughrabi, "Fatigue, an Everlasting Materials Problem—Still En Vogue," *Procedia Engineering* 2, no. 1 (2010): 3–26.

2. S. Suresh, *Fatigue of Materials* (Cambridge University Press, 1998).

3. R. I. Stephens, A. Fatemi, R. R. Stephens, and H. O. Fuchs, *Metal Fatigue in Engineering* (John Wiley & Sons, 2000).

4. D. F. Socie and G. B. Marquis, *Multiaxial Fatigue* (Society of Automotive Engineers International, 2000).

5. W. Cui, "A State-of-the-Art Review on Fatigue Life Prediction Methods for Metal Structures," *Journal of Marine Science and Technology* 7, no. 1 (2002): 43–56.

6. A. Fatemi and D. F. Socie, "A Critical Plane Approach to Multiaxial Fatigue Damage Including Out-of-Phase Loading," *Fatigue & Fracture of Engineering Materials & Structures* 11, no. 3 (1988): 149–165.

7. M. Borodii and S. Shukaev, "Additional Cyclic Strain Hardening and Its Relation to Material Structure, Mechanical Characteristics, and Lifetime," *International Journal of Fatigue* 29, no. 6 (2007): 1184–1191.

8. J. Papuga, "A Survey on Evaluating the Fatigue Limit Under Multiaxial Loading," *Journal of Fatigue* 33, no. 2 (2011): 153–165.

9. A. Fatemi and N. Shamsaei, "Multiaxial Fatigue: An Overview and Some Approximation Models for Life Estimation," *International Journal of Fatigue* 33, no. 8 (2011): 948–958.

10. D. F. Socie, "Fatigue-Life Prediction Using Local Stress–Strain Concepts," *Experimental Mechanics* 17, no. 2 (1977): 50–56.

11. Y. Zeng, M. Li, H. Wu, N. Li, and Y. Zhou, "Experiment and Theoretical Investigation on Fatigue Life Prediction of Fracturing Pumpheads Based on a Novel Stress-Field Intensity Approach," *Materials* 15, no. 13 (2022): 4413.

12. X. Chen, S. Xu, and D. Huang, "A Critical Plane-Strain Energy Density Criterion for Multiaxial Low-Cycle Fatigue Life Under Non-Proportional Loading," *Fatigue & Fracture of Engineering Materials & Structures* 22, no. 8 (1999): 679–686.

13. A. Ince and G. Glinka, "A Generalized Fatigue Damage Parameter for Multiaxial Fatigue Life Prediction Under Proportional and Non-Proportional Loadings," *International Journal of Fatigue* 62 (2014): 34–41.

14. L. Gan, H. Wu, and Z. Zhong, "Multiaxial Fatigue Life Prediction Based on a Simplified Energy-Based Model," *International Journal of Fatigue* 144 (2021): 106036.

15. J. Hoffmeyer, R. Döring, T. Seeger, and M. Vormwald, "Deformation Behaviour, Short Crack Growth and Fatigue Lives Under Multiaxial Nonproportional Loading," *International Journal of Fatigue* 28, no. 5/6 (2006): 508–520.

16. D. Shang, G. Sun, J. Deng, and C. Yan, "Multiaxial Fatigue Damage Parameter and Life Prediction for Medium-Carbon Steel Based on the Critical Plane Approach," *International Journal of Fatigue* 29, no. 12 (2007): 2200–2207.

17. J. W. Doong, M. R. Hill, and D. F. Socie, "Nonproportional Cyclic Deformation and Fatigue of 1045 Steel," *Journal of Engineering Materials and Technology* 113, no. 1 (1991): 23–30.

18. J. L. Chaboche, "A Review of Some Plasticity and Viscoplasticity Constitutive Theories," *International Journal of Plasticity* 24, no. 10 (2008): 1642–1693.

19. A. Mishra, C. Anitescu, P. R. Budarapu, S. Natarajan, P. R. Vundavilli, and T. Rabczuk, "An Artificial Neural Network-Based Deep Collocation Method for the Solution of Transient Linear and Nonlinear Partial Differential Equations," *Frontiers of Structural and Civil Engineering* 18, no. 8 (2024): 1296–1310.

20. K. Pałczyński, D. Skibicki, Pejkowski, and T. Andrysiak, "Application of Machine Learning Methods in Multiaxial Fatigue Life Prediction," *Fatigue & Fracture of Engineering Materials & Structures* 46, no. 2 (2022): 416–432.

21. J. Yang, G. Kang, and Q. Kan, "A Novel Deep Learning Approach of Multiaxial Fatigue Life Prediction With a Self-Attention Mechanism Characterizing the Effects of Loading History and Varying Temperature," *International Journal of Fatigue* 162 (2022): 106851.

22. Z. Zhan, X. He, D. Tang, et al., "Recent Developments and Future Trends in Fatigue Life Assessment of Additively Manufactured Metals With Particular Emphasis on Machine Learning Modeling," *Fatigue & Fracture of Engineering Materials & Structures* 46, no. 12 (2023): 4425–4464.

23. E. Samaniego, C. Anitescu, S. Goswami, et al., "An Energy Approach to the Solution of Partial Differential Equations in Computational Mechanics via Machine Learning: Concepts, Implementation and Applications," *Computer Methods in Applied Mechanics and Engineering* 362 (2020): 112790.

24. A. Karolczuk, J. Papuga, and T. Palin-Luc, "Progress in Fatigue Life Calculation by Implementing Life-Dependent Material Parameters in Multiaxial Fatigue Criteria," *International Journal of Fatigue* 134 (2020): 105509.

25. Q. Y. Deng, S. P. Zhu, X. Niu, G. Lesiuk, W. Macek, and Q. Wang, "Load Path Sensitivity and Multiaxial Fatigue Life Prediction of Metals Under Non-Proportional Loadings," *International Journal of Fatigue* 166 (2023): 107281.

26. S. Chen, Y. Bai, X. Zhou, and A. Yang, "A Deep Learning Dataset for Metal Multiaxial Fatigue Life Prediction," *Scientific Data* 11 (2024): 1027.

27. G. Abed, Y. L. Lee, J. Quigley, and W. Zhang, "Assessment of the Poisson Ratio Effect on Low Cycle Fatigue (LCF) Behavior of Shear-Cracking Mode Materials," *Journal of Testing and Evaluation* 44, no. 4 (2016): 1509–1524.

28. N. Vu-Bac, A. H. Nguyen, and V. H. Luong, "Uncertainty Analysis of Static Fatigue of Hi-Nicalon Bundles," *Engineering Analysis With Boundary Elements* 167 (2024): 6.

29. N. Vu-Bac, X. Zhuang, and T. Rabczuk, "Uncertainty Quantification for Mechanical Properties of Polyethylene Based on Fully Atomistic Model," *Materials* 12 (2019): 13.

30. N. Vu-Bac, M. Silani, T. Lahmer, X. Zhuang, and T. Rabczuk, "A Unified Framework for Stochastic Predictions of Mechanical Properties of Polymeric Nanocomposites," *Computational Materials Science* 96 (2015): 520–535.

31. I. M. Sobol, "Sensitivity Estimates for Nonlinear Mathematical Models," *Mathematical Modeling and Computational Experiment* 1, no. 4 (1993): 407–414.

32. A. Saltelli, M. Ratto, T. Andres, et al., *Global Sensitivity Analysis: The Primer* (Wiley, 2008).

33. N. Vu-Bac, R. Rafiee, X. Zhuang, T. Lahmer, and T. Rabczuk, "Uncertainty Quantification for Multiscale Modeling of Polymer Nanocomposites With Correlated Parameters," *Composites B* 68 (2015): 446–464.

34. S. Kucherenko, S. Tarantola, and P. Annoni, "Estimation of Global Sensitivity Indices for Models With Dependent Variables," *Computer Physics Communications* 183, no. 4 (2012): 937–946.

35. C. Xu and G. Z. Gertner, "Uncertainty and Sensitivity Analysis for Models With Correlated Inputs," *Reliability Engineering & System Safety* 93, no. 10 (2008): 1563–1573.

36. S. M. Dsouza, T. M. Varghese, P. R. Budarapu, and S. Natarajan, "A Non-Intrusive Stochastic Isogeometric Analysis of Functionally Graded Plates With Material Uncertainty," *Axioms* 9, no. 3 (2020): 92.

37. K. M. Hamdia, M. A. Msekh, M. Silani, T. Q. Thai, P. R. Budarapu, and T. Rabczuk, "Assessment of Computational Fracture Models Using Bayesian Method," *Engineering Fracture Mechanics* 205 (2019): 387–398.

38. A. I. J. Forrester and A. J. Keane, "Recent Advances in Surrogate-Based Optimization," *Progress in Aerospace Sciences* 45, no. 1/3 (2009): 50–79.

39. G. G. Wang and S. Shan, "Review of Metamodeling Techniques in Support of Engineering Design Optimization," *Journal of Mechanical Design* 129, no. 4 (2006): 370–380.

40. T. C. H. Nguyen, N. Vu-Bac, and P. R. Budarapu, "A Kriging-Based Uncertainty Quantification for Fracture Assessment," *International Journal of Computational Methods* 22 (2024): 01.

41. Z. Li, H. Yue, C. Zhang, et al., "Fatigue Life Prediction of 2024-T3 Al Alloy by Integrating Particle Swarm Optimization—Extreme Gradient Boosting and Physical Model," *Materials* 17, no. 21 (2024): 5332.

42. S. K. Dasari, A. Cheddad, and P. Andersson, "Random Forest Surrogate Models to Support Design Space Exploration in Aerospace Use-Case," in *Artificial Intelligence Applications and Innovations (AIAI 2019)*, Vol. 559, ed. J. MacIntyre, I. Maglogiannis, L. Iliadis, and E. Pimenidis, IFIP Advances in Information and Communication Technology (Springer, 2019), 532–544.

43. N. V. Queipo, R. T. Haftka, W. Shyy, T. Goel, R. Vaidyanathan, and P. K. Tucker, "Surrogate-Based Analysis and Optimization," *Progress in Aerospace Sciences* 41, no. 1 (2005): 1–28.

44. S. Shahane, E. Guleryuz, D. W. Abueidda, et al., "Surrogate-Based Analysis and Optimization," *Computers & Structures* 270 (2022): 106843.

45. K. Cheng, Z. Lu, C. Ling, and S. Zhou, "Surrogate-Assisted Global Sensitivity Analysis: An Overview," *Structural and Multidisciplinary Optimization* 61, no. 3 (2020): 1187–1213.

46. N. Vu-Bac, T. Lahmer, X. Zhuang, T. Nguyen-Thoi, and T. Rabczuk, "A Software Framework for Probabilistic Sensitivity Analysis for Computationally Expensive Models," *Advances in Engineering Software* 100 (2016): 19–31.

47. O. H. Basquin, "The Exponential Law of Endurance Tests," *Proceedings of the American Society for Testing Materials* 10 (1910): 625–630.

48. J. Polák, "Role of Persistent Slip Bands and Persistent Slip Markings in Fatigue Crack Initiation in Polycrystals," *Crystals* 13, no. 2 (2023): 220.

49. H. Mughrabi, "Microstructural Mechanisms of Cyclic Deformation, Fatigue Crack Initiation and Early Crack Growth," *Philosophical Transactions of the Royal Society A: Mathematical, Physical and Engineering Sciences* 373, no. 2038 (2015): 20140132.

50. L. Breiman, "Random Forests," *Machine Learning* 45, no. 1 (2001): 5–32.

51. T. Chen and C. Guestrin, "XGBoost: A Scalable Tree Boosting System," Paper presented at the 22nd ACM SIGKDD International Conference on Knowledge Discovery and Data Mining, August 13–17, San Francisco, CA, 2016, accessed April 9, 2025, https://doi.org/10.1145/2939672.2939785.

52. H. Nasiri, A. Dadashi, and M. Azadi, "Machine Learning for Fatigue Lifetime Predictions in 3D-printed Polylactic Acid Biomaterials Based on Interpretable Extreme Gradient Boosting Model," *Materials Today Communications* 39 (2024): 109054.

53. A. Saltelli, P. Annoni, I. Azzini, F. Campolongo, M. Ratto, and S. Tarantola, "Variance Based Sensitivity Analysis of Model Output. Design and Estimator for the Total Sensitivity Index," *Computer Physics Communications* 181, no. 2 (2010): 259–270.

54. I. Papaioannou and D. Straub, "Variance-Based Reliability Sensitivity Analysis and the FORM α-Factors," *Reliability Engineering & System Safety* 210 (2021): 107496.